Supplementary Material for

Topological Landau-Zener Nanophotonic Circuits

Bing-Cong Xu,[a,†] Bi-Ye Xie,[b,†] Li-Hua Xu,[c,†] Ming Deng,[a] Weijin Chen[d], Heng Wei[d], Feng-Liang Dong,[c,e,*] Jian Wang,[a] Cheng-Wei Qiu[d,*], Shuang Zhang,[f,*] and Lin Chen[a,g,*]

[a]Wuhan National Laboratory for Optoelectronics and School of Optical and Electronic Information, Huazhong University of Science and Technology, Wuhan 430074, China

[b]School of Science and Engineering, The Chinese University of Hong Kong, Shenzhen, 518172, China

[c]Nanofabrication Laboratory, CAS Key Laboratory for Nanosystems and Hierarchical Fabrication, CAS Key Laboratory for Nanophotonic Materials and Devices, CAS Center for Excellence in Nanoscience, National Center for Nanoscience and Technology of China Beijing 100190, China

[d]Department of Electrical and Computer Engineering, National University of Singapore, Singapore 117583, Singapore

[e]Center of Materials Science and Optoelectronics Engineering, University of Chinese Academy of Sciences, Beijing 100049, China

[f]Department of Physics, The University of Hong Kong, Hong Kong, China

[g]State Key Laboratory for Mesoscopic Physics, School of Physics, Peking University, Beijing 100871, China

* Correspondence authors

† These authors contributed equally to this work

Contents

1. Calculation of coupling coefficient

The coupling coefficient is related to the overlapping integral of mode fields between two near-neighbor waveguides. It also characterizes the transfer rate of light field energy between waveguides. The coupling coefficient can also be defined by the coupling length L_c, i. e., the shortest distance required for the maximum proportional transfer of light field energy from one waveguide to another. The coupling coefficient can be calculated with

$$C = \sqrt{\frac{\pi^2}{4L_c^2} - \Delta k^2} \tag{S1}$$

where $\Delta k = k_1 - k_2$ is the detuning in propagation constant[50]. We can get the coupling length L_c and the propagation constant k of a single waveguide by simulating the light field in two waveguides with Lumerical FDTD-Solutions.

2. The tunneling probability predicted by LZ model

LZ model predicts the final states of the evolution process in the middle panel of Fig. 1d. It mainly depends on the speed of evolution which is strongly governed by the size of band gap Δk and decay speed of band gap, i.e., the slope of the energy level α around degenerate point $\beta_x = 0.75\pi$. The evolution speed here is set to be $\delta\beta_x/L$, where L is the device length in Fig. 2a. The finial state is given by the following dynamical eigen equations[31,39]

$$-i\frac{d}{dx}\begin{bmatrix} S_1(x) \\ S_2(x) \end{bmatrix} = \begin{bmatrix} \alpha\delta\beta_x x/L & \delta k/2 \\ \delta k/2 & -\alpha\delta\beta_x x/L \end{bmatrix}\begin{bmatrix} S_1(x) \\ S_2(x) \end{bmatrix} \tag{S2}$$

The finial state can be written as $\left|\varphi_f\right\rangle = S_1(z)\left|\varphi_1\right\rangle + S_2(z)\left|\varphi_2\right\rangle$, where $\left|\varphi_1\right\rangle$ and $\left|\varphi_2\right\rangle$ are the two states involved in LZ model. By solving Eq. (S2), we find the tunneling probability can be written as $S_1{}^2(L) = e^{[-\pi(\delta k)^2 L/4\alpha\delta\beta_x]}$, if the initial state is $\left|\varphi_2\right\rangle$. The LZ tunneling and LZ single-band evolution share equal probability when the device length is $4\alpha\delta\beta_x \ln(2)/\pi\left(\delta k\right)^2$ in the main text. This device length is regarded as the equal-probability distance of single-band evolution and non-adiabatic tunneling.

3. The structural parameters of the device for edge-to-edge channel conversion

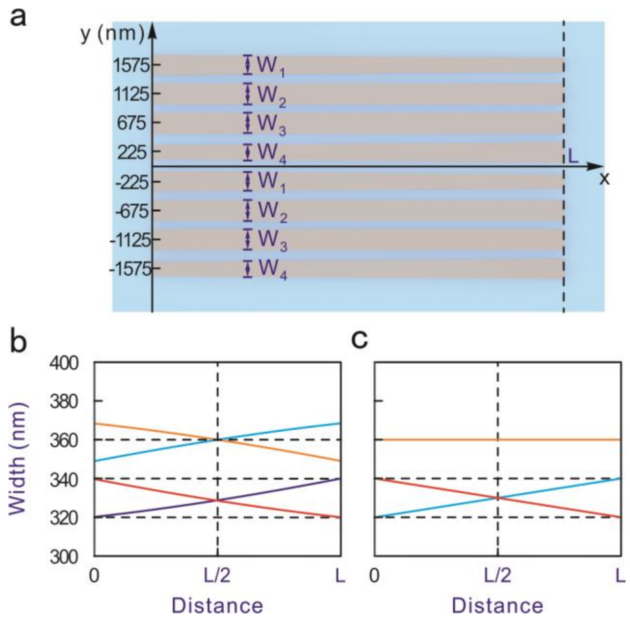

Fig. S1 The structural parameters of the device for TESs edge-to-edge channel conversion. a, The top view of the eight-waveguide array. **b**, The width of four waveguides versus propagation distance in a unit cell with Harper model. The red, orange, blue and purple lines represent W_1, W_2, W_3 and W_4, respectively. **c**, The width of four waveguides versus propagation distance in a unit cell with linear model. The red and blue lines correspond to W_1 and W_4, respectively, while W_2 and W_3 share the same orange line.

4. Calculation of the topological invariants

For calculating Zak phase of a 1D topological insulator and the Chern number of a 2D Chern insulator, the Berry connection is taken into account. In this section, we will detailly show how to use Wilson loop within the two-dimensional $\beta_x \beta_y$ plane to retrieve the Chern number.

First, the classic 2D Berry connection is defined as[51]

$$\mathbf{a}_n(\boldsymbol{\beta}) = i\langle \mu_n(\boldsymbol{\beta})|\nabla_{\boldsymbol{\beta}}|\mu_n(\boldsymbol{\beta})\rangle \tag{S3}$$

It is known that, the gauge transformation, i.e., $|\mu_n(\boldsymbol{\beta})\rangle \to |\mu_n(\boldsymbol{\beta})\rangle e^{i\alpha}$ with random $\alpha \in [0, 2\pi)$, doesn't influence the eigen equations of the system, but which largely breaks the continuity of the wave function $|\mu_n(\boldsymbol{\beta})\rangle$. The conventional method of calculating the Berry phase of the n-th band,

$$\Phi_{B,n} = \int_{FBZ} (\nabla \times \mathbf{a}_n(\boldsymbol{\beta})) d\mathbf{S} \tag{S4}$$

is invalid. To simplify the calculation of Berry phase, we divide the integral area into P small subblocks Γ_p and use the Stokes formula to convert the surface integral of Berry curvature to a closed loop line integral of Berry connection in every block. Then (S4) can be rewritten as

$$\Phi_{B,n} = \sum_{p=1}^{P} \int_{\Gamma_p} \mathbf{a}_n(\boldsymbol{\beta}) d\boldsymbol{\beta} \tag{S5}$$

Until this step, we still cannot avoid the issue caused by the discontinuity of the wave function under the gauge transformation. We can then discretize Eq. (S5), and take complex exponent, resulting in a multiplication expression

$$e^{-i\Phi_{B,n}} = \prod_{p=1}^{P} e^{\left[\int_{\Gamma_p} (\langle \mu_n(\boldsymbol{\beta})|\nabla|\mu_n(\boldsymbol{\beta})\rangle) d\boldsymbol{\beta}\right]} \tag{S6}$$

If each divided subblock is small enough, i.e., $P \to \infty$, the condition of Taylor expansion will be satisfied. With further segmentation of subblock boundaries to Q_p parts, we can get

$$e^{-i\Phi_{B,n}}=\prod_{p=1}^{P}\prod_{q=1}^{Q_p}(1+\langle\mu_n(\boldsymbol{\beta}_q)|\nabla|\mu_n(\boldsymbol{\beta}_q)\rangle d\boldsymbol{\beta}) \tag{S7}$$

Finally, the gradient operator can be represented in a differential form

$$e^{-i\Phi_{B,n}}=\prod_{p=1}^{P}\prod_{q=1}^{Q_p}(1+\langle\mu_n(\boldsymbol{\beta})|(\frac{|\mu_n(\boldsymbol{\beta}_{q+1})\rangle-|\mu_n(\boldsymbol{\beta}_q)\rangle}{|d\boldsymbol{\beta}|})d\boldsymbol{\beta}) \tag{S8}$$

Since the system is Hermitian, the Bloch eigenstates are orthogonal, i.e., $\langle\mu_n(\boldsymbol{\beta}_q)|\mu_n(\boldsymbol{\beta}_q)\rangle=1$. Equation (S8) is further rewritten as

$$e^{-i\Phi_{B,n}}=\prod_{p=1}^{P}(\langle\mu_n(\boldsymbol{\beta}_1)|\mu_n(\boldsymbol{\beta}_2)\rangle\ldots\langle\mu_n(\boldsymbol{\beta}_q)|\mu_n(\boldsymbol{\beta}_{q+1})\rangle\ldots\langle\mu_n(\boldsymbol{\beta}_{Q_p})|\mu_n(\boldsymbol{\beta}_1)\rangle) \tag{S9}$$

The Wilson loop is just the multiplication expression along subblock boundaries. Note that Eq. (S9) is invariant under the gauge transformation with the existence of term $|\mu_n(\boldsymbol{\beta}_q)\rangle\langle\mu_n(\boldsymbol{\beta}_q)|$. Thus, one can calculate the Berry phase by use of concatenated multiplication of Wilson loops on discrete subblocks, rather than integral on continuous parameter space. The Chern number is thus retrieved as it is associated to the Berry phase with

$$C_n=\frac{\Phi_{B,n}}{2\pi} \tag{S10}$$

For 1D insulators, one can simply use numerical integration over the entire First Brillouin zone to retrieve Zak phase without requiring to discretize the parameter space

$$\Phi_{Z,n}=i\int_{FBZ}\langle\mu_n(\beta)|\frac{\partial}{\partial\beta}|\mu_n(\beta)\rangle d\beta \tag{S11}$$

In this work, we have used the method in this section to avoid the random phase related to the gauge transformation. The Chern number of our four-level Harper model in Fig. 2d and the Zak phase of the one-dimensional insulators in Fig. 2b of the main text are calculated based on this section. It is worth noticing that the second and third band are degenerate in Fig. 2d. We cannot calculate the Chern numbers of them directly. But we can regard them as a single band with a common Chern number. We can first calculate the sum of the other band Chern numbers. The common Chern number of the two degenerate bands is the opposite number of this sum.

5. Bulk Momentum-Space Hamiltonian of four-level model

We use the internal and external degrees of freedom m, n to characterize the states of the multi-level chain with the following definition

$$|m,n\rangle = |m\rangle \otimes |n\rangle \tag{S12}$$

where $|m,n\rangle$ denotes the state on the n-th site in the m-th unit cell, and is expressed by the Kronecker product of two vectors $|m\rangle$ and $|n\rangle$. $|m\rangle$ and $|n\rangle$ represent the m-dimensional and n-dimensional column vector, respectively. For a four-level chain, n is equal to 4, yielding

$$|m\rangle = \overbrace{\left[0,0,0,...,0,\underset{m-\text{th}}{1},0,...,0,0,0\right]}^{M}, \quad (m=1,2,...,M) \tag{S13}$$

$$|n\rangle = \left[0,\underset{n-\text{th}}{1},0,0\right], \quad (n=1,2,3,4) \tag{S14}$$

The real space bulk Hamiltonian can thus be written as Eq. (1) in the main text.

Based on the definition mentioned above, the momentum-space Hamiltonian $H(\beta_y)$ can be extracted by Fourier transformation, which is essentially a linear transformation and can be regarded as the matrix row and column transformation. According to the Bloch theorem, the periodical potential field's wavefunction can be decomposed into linearly superimposed plane waves (basic states). The Fourier transformation is only applied to the external degree of freedom[43], and the transition vector is given as

$$|\beta_y\rangle = \frac{1}{\sqrt{M}}\sum_{m=1}^{M} e^{im\beta_y}|m\rangle, \quad (\beta_y \in \{\frac{2\pi}{M},\frac{4\pi}{M},...,2\pi\}) \tag{S15}$$

The bulk momentum-space Hamiltonian can be obtained by the following Matrix transformation

$$H(\beta_y) = \sum_{n,n'\in\{1,2,3,4\}} \langle \beta_y, n|\hat{H}_{bulk}|\beta_y, n'\rangle \cdot |n\rangle\langle n'| \tag{S16}$$

$$H(\beta_y)k(\beta_y) = k(\beta_y)\left|\mu_y(\beta_y)\right\rangle \tag{S17}$$

With the same definition of the parameters in Eq. (1), the bulk momentum-space Hamiltonian is transformed to

$$H(\beta_y) = \begin{bmatrix} 0 & C_{12} & 0 & C_{41}e^{-i\beta_y} \\ C_{12} & 0 & C_{23} & 0 \\ 0 & C_{23} & 0 & C_{34} \\ C_{41}e^{i\beta_y} & 0 & C_{34} & 0 \end{bmatrix} \tag{S18}$$

The eigenvalues $k(\beta_y)$ of $H(\beta_y)$ make up the system's Bloch band. The eigenstates $\left|\mu_n(\beta_y)\right\rangle$ are used to calculate the topological invariants in Section 4. If the periodical detuning $k_n(\beta_x) = k_b + \Delta k \cos(\beta_x + \pi n/2)$ is exerted to modulate the one-dimensional model (see the main text), the bulk momentum-space Hamiltonian becomes a binary matrix function, corresponding to the $\beta_x\,\beta_y$ plane,

$$H(\beta_x, \beta_y) = \begin{bmatrix} k_1(\beta_x) & C_{12} & 0 & C_{41}e^{-i\beta_y} \\ C_{12} & k_2(\beta_x) & C_{23} & 0 \\ 0 & C_{23} & k_3(\beta_x) & C_{34} \\ C_{41}e^{i\beta_y} & 0 & C_{34} & k_4(\beta_x) \end{bmatrix} \tag{S19}$$

By solving its eigenvalues, we can obtain the spectrum on the propagation constant versus β_x and β_y in the 2D parameter space in Fig. 2d.

6. Simulated edge-to-edge channel conversion efficiency of TESs

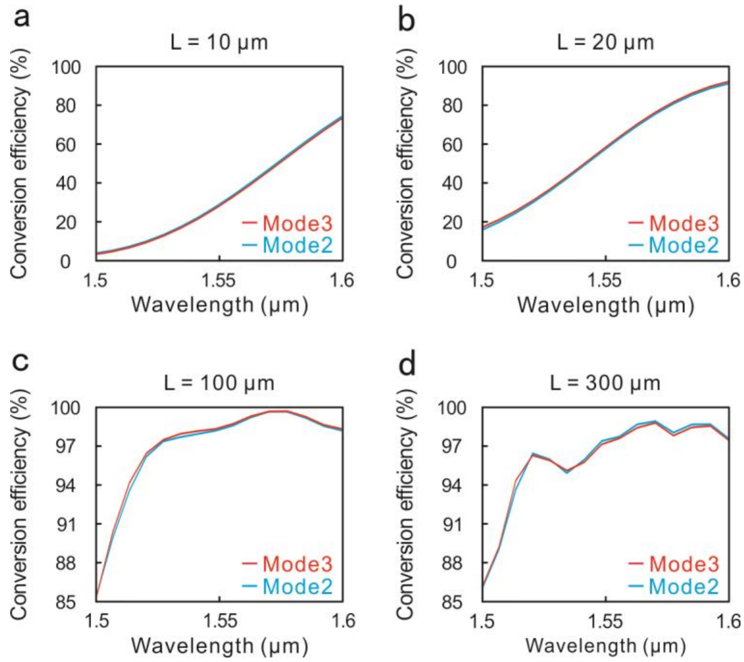

Fig. S2 The simulated topological edge states (TESs) edge-to-edge channel conversion efficiency. a-d, Linear model in Fig. S1c with $L = 10$ μm **(a)**, $L = 20$ μm **(b)**, $L = 100$ μm **(c)**, and $L = 300$ μm **(d)**. Red (blue) line represents the edge-to-edge channel conversion efficiency of mode 3 (mode 2).

The edge-to-edge channel conversion efficiency is defined as the ratio of the desired output mode energy to the total energy. As is shown in Fig. S2, the edge-to-edge channel conversion efficiencies are on the level about only 26% at the wavelength center $\lambda = 1.55$ μm when the device length is only $L = 10$ μm. If the device length is approaching to the equal-probability distance ($x_c = 16.9$ μm) with $L = 20$ μm, the edge-to-edge channel conversion efficiencies increase to the level of 56% at the wavelength center $\lambda = 1.55$ μm. It indicates almost the same probability of tunneling and adiabatic edge-to-edge channel conversion. The edge-to-edge channel conversion efficiencies maintain high levels over 93% in the wavelength range greater than 1.52 μm at two studied device lengths of $L = 100$ μm and $L = 300$ μm ($> x_c = 16.9$ μm). The modes 2 and 3 obtain almost the same edge-to-edge channel conversion efficiencies, indicating a bilateral and efficient edge-to-edge channel conversion. The overall edge-to-edge channel conversion efficiency with linear mode ensures high edge-to-edge channel conversion efficiency under the adiabatic limit, demonstrating a good tolerance against the structural parameters.

It is worth pointing out here, LZ channel converters can serve as wavelength-dependent switches by tuning the operating wavelength to govern whether or not the field jumps between edges, when the device length L is less than or comparable to x_c. For example, as the working wavelength is chosen to be 1.5 μm, the tunneling process dominates and most of light will propagate along one edge. In contrast, as the working wavelength approaches to 1.6 μm, most of the light energy goes through a Landau-Zener single-band evolution, and can switch to the opposite edge.

7. Experimental details

The experimental fabrication of the waveguide array was implemented by using a standard silicon-on-insulator wafer with a 220 nm-thick silicon layer, followed by E-beam lithography and inductively coupled plasma etching. A layer of 2 μm-thick silica dioxide serves as the cladding layer on the silicon waveguide to improve the symmetry of the optical field and protect the silicon structures.

7.1. Grating coupler

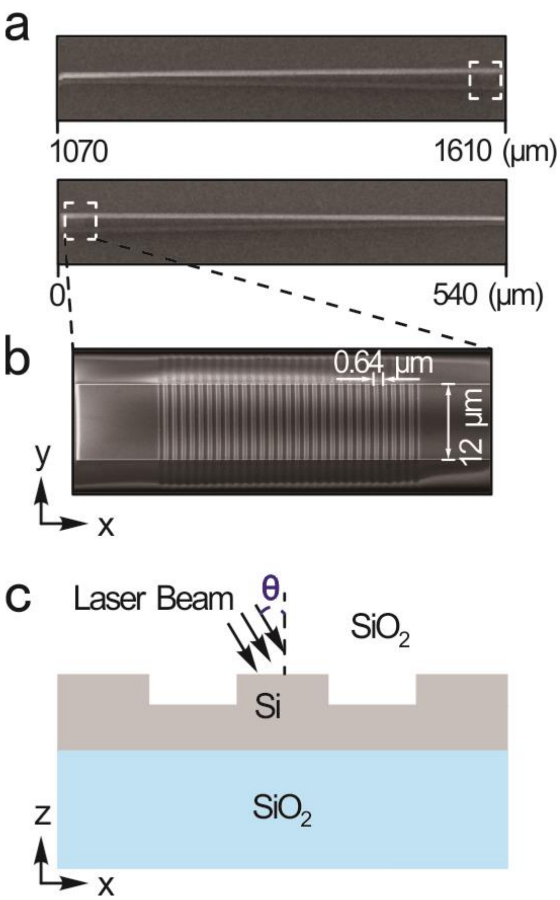

Fig. S3 The silicon grating coupler for measurement. a, SEM image for section A or E in Fig. 4a. **b**, SEM image of the silicon couple-in/couple-out grating coupler with its cross section (**c**). The incident light illuminates the grating with angle of θ with respect to the normal direction.

The grating coupler is designed to couple into the silicon waveguide from the laser beam or couple out light energy that is received spectrometer and power meter. The grating has a period of $l = 640$ nm and a width of 12 μm, with a duty cycle of 0.5. The etching depth for the grating is with 100 nm, which is optimized for the maximum coupling efficiency. The incident angle θ is chosen as the maximum power is detected by the power meter. The silicon waveguide is connected with the silicon grating, and its width is linearly changed from 12 μm to 340 nm or to 320 nm with a total distance of 540 μm.

7.2. Adiabatic coupler

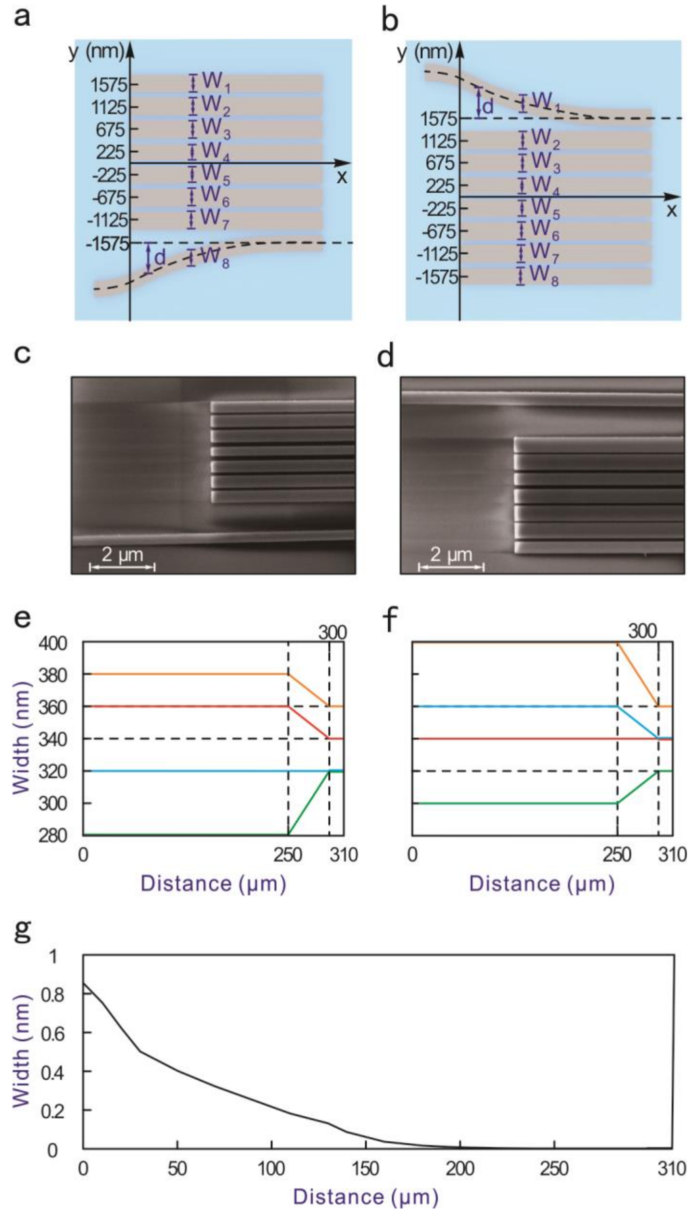

Fig. S4 The adiabatic coupler for section B in Fig. 4a. a-b, The top-view schematic of the adiabatic coupler for exciting the TESs: mode 2 (**a**) and mode 3 (**b**). **c-d**, SEM images of the starting sections: (**c**) and (**d**) correspond to (**a**) and (**b**), respectively. **e**, The waveguide width versus the propagation distance in (**a**). The red, orange, green, and blue lines denote W_1 $(=W_5)$, W_2 $(=W_3=W_6=W_7)$, W_4, and W_8. **f**, The waveguide width versus the propagation distance in (b). The red, orange, green, and blue lines denote W_1, W_2 $(=W_3=W_6=W_7)$, $W_4=W_8$, and W_5. **g**, The off-axis distance d of waveguide 1 (**b**) and waveguide 8 (**a**) versus the propagation distance.

The adiabatic coupler presented in Fig. S4 is used to gradually convert the silicon waveguide mode to the TESs for Section C in Fig. 4a. The off-axis distance d is adiabatically modulated along the propagating distance (300 μm in length) to ensure the excitation of mode 2 (mode 3) with a high mode purity. The optimized structural parameters for the adiabatic coupler are shown in Figs. S4e-g, resulting in an excited mode 2 (mode 3) with a mode purity above 97% in simulation.

7.3. Measurement configuration

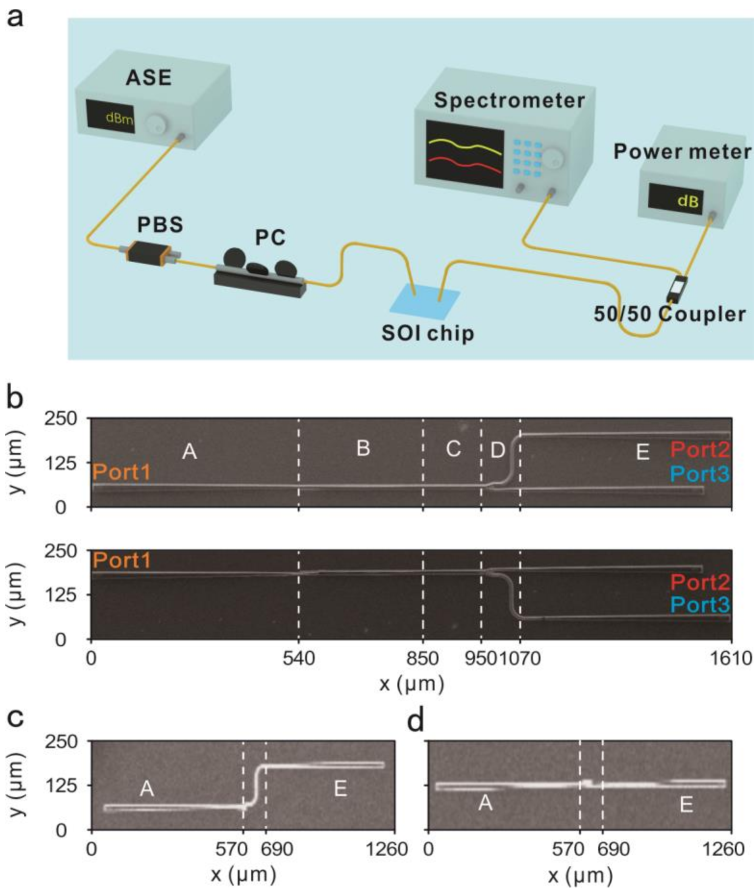

Fig. S5 Details on measurement. a, Measurement configuration. **b-d**, SEM images of the silicon waveguide array for TESs conversion: The entire device involving the silicon waveguide array (**b**), The contrast waveguides in the absence of silicon waveguide array (**c-d**).

Figure S5a presents the experimental setup for measuring the TESs conversion effect. The near infrared light is provided by an amplified spontaneous emission (ASE) broadband light source (Amonics ALS-CL-15-B-FA, spectral range from 1528 nm to 1608 nm). The polarization beam splitter (PBS) and polarization controller (PC) are used to adjust the polarization of the incident light for mode matching with the grating coupler. The optical field after passing through the waveguide array is coupled out of the silicon waveguide and then collected by the optical power meter (AV633 4D) and spectrometer (YOKOGAWA AQ6370). The SEM images of the entire device involving the silicon waveguide array for mode 3 conversion (upper panel of Fig. S5b) and mode

2 conversion (lower panel of Fig. S5b) are presented in the upper and lower panels in Fig. S5b, respectively. Sections A and E are the grating couplers for coupling in and out of the waveguide energy, respectively. Section B corresponds to the adiabatic coupler for exciting the TESs, and section D represents the bus waveguide array for testing the edge-to-edge channel conversion effect. The contrast waveguides in Figs. S5c-d are designed to evaluate the additional loss generated by the grating coupler structure on both sides. The optical power at port 2 (port 3) I_2 (I_3) in the upper panel of Fig. S5b, is extracted by comparing the device losses between the port 2 (port 3) and the contrast waveguide in Fig. S5c (Fig. S5d). The optical power at port 2 (port 3) I_2 (I_3) in the lower panel of Fig. S5b, is extracted by comparing the device losses between the port 2 (port 3) and the contrast waveguide in Figs. S5d (Fig. S5c).

8. The robustness against the fabrication errors

8.1. Theoretical analysis

We note the robustness of a system against perturbation in most previous works was studied by use of Anderson perturbation appearing at random sites. For practical preparation of nanoscale structures, the fabrication error largely comes from the pattern technologies, and high-resolution E-beam lithography is mostly used for the current nanoscale silicon waveguide array[52]. As the height of the silicon waveguide is fixed, its perturbation in fabrication process is decided by the holistic width perturbation of waveguides, rather than the perturbation at random sites[53-55]. Here, we resort to directly studying the topological transition points due to the limited waveguide lattice used in Fig. 2a.

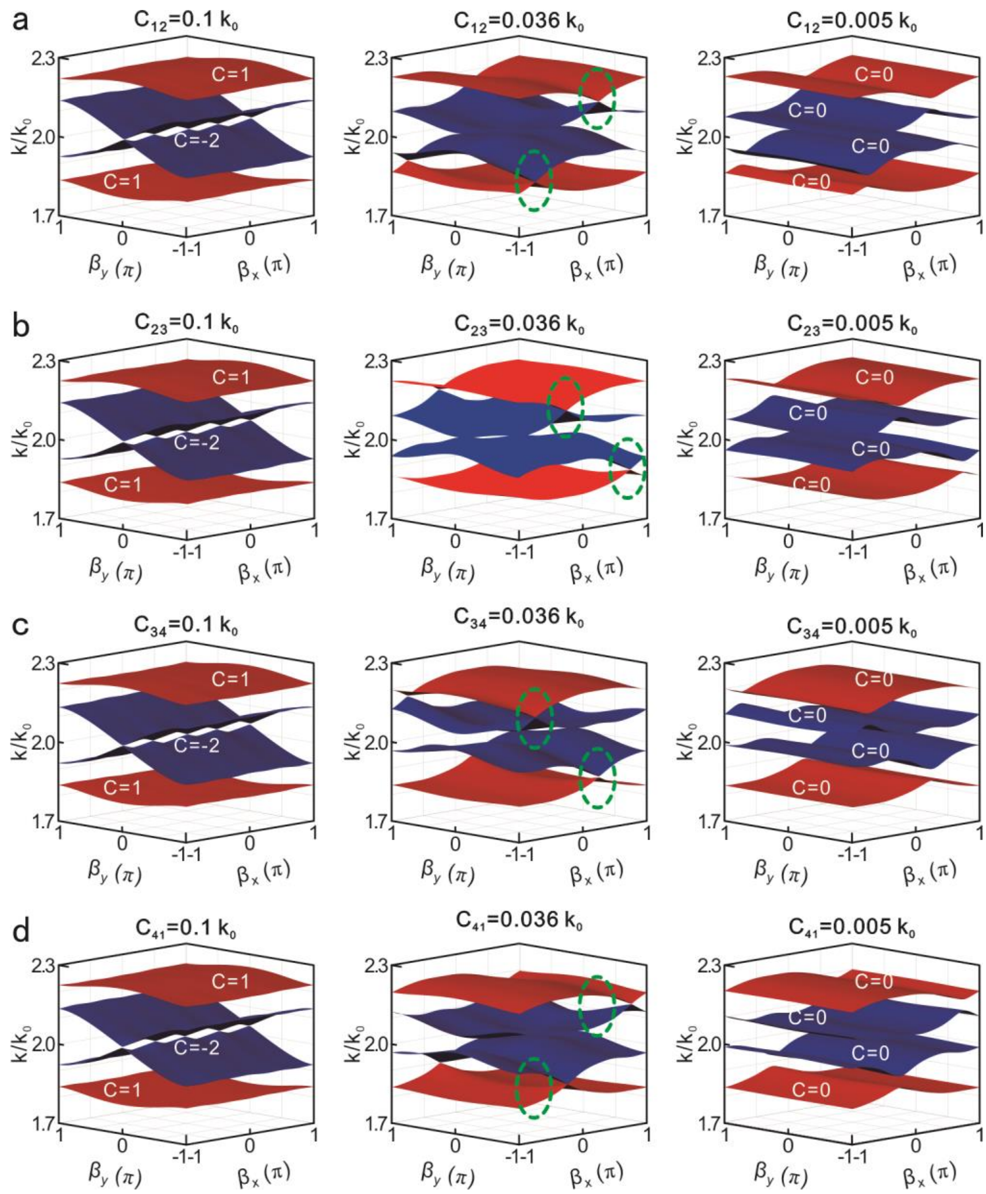

Fig. S6 The topological invariant of four Bloch bands as a function of the coupling coefficients. **a**, C_{12} is varied with fixed $C_{23} = C_{34} = C_{41} = 0.1\,k_0$. **b**, C_{23} is varied with fixed $C_{12} = C_{34} = C_{41} = 0.1\,k_0$. **c**, C_{34} is varied with fixed $C_{12} = C_{23} = C_{41} = 0.1\,k_0$. **d**, C_{41} is varied with fixed $C_{12} = C_{23} = C_{34} = 0.1k_0$.

In the main text, the Chern numbers of the Harper waveguide lattice in Fig.2a has been calculated as all the coupling coefficients are fixed at $C_{12} = C_{34} = C_{41} = C_{41} = 0.1k_0$. We take the coupling coefficients, C_{12}, C_{23}, C_{34}, and C_{41} as the independent variables to calculate the topological phase transition point of the Harper waveguide lattice. Figures S6a-d, respectively show the topological phase suffers from a process transforming from non-trivial phase to trivial phase as each coupling coefficient is individually changed. The topological phase transition points are identical and very close to zero with $C_{12} = 0.036\,k_0$ (Fig. S6a), $C_{23} = 0.036\,k_0$ (Fig. S6b), $C_{34} = 0.036\,k_0$ (Fig. S6c), $C_{41} = 0.036\,k_0$ (Fig. S6d). All the coupling coefficients in our system can be varied within a wide range to support TESs. The topological phase transition point indicates the critical point in $C_{n,(n \bmod 4)+1}$ axis between trivial phase and non-trivial phase. In our case, the coupling coefficients are strongely related to the gap distance beween the waveguides, $g_{n,(n \bmod 4)+1}$, in the array. The presented four-level system with Harper waveguide lattice can support TESs evolution even if $C_{n,(n \bmod 4)+1}$ are varied within a wide range ($> 0.036\,k_0$), allowing for a wide range of $g_{n,(n \bmod 4)+1}$ in the design.

8.2. Experimental validation

We have experimentally revealed the device robustness against the structural parameters by tuning the gap between the unit cell, g_{41}.

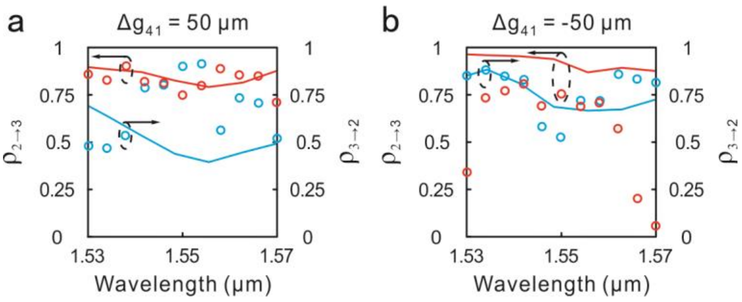

Fig. S7 The experimental results for testing robustness. The simulated and experimental power contrast ratio $\rho_{2\to3}$, $\rho_{3\to2}$ versus light wavelength with $\Delta g_{41} = 50\ \text{nm}$ (**a**) and $\Delta g_{41} = -50\ \text{nm}$ (**b**), when L is kept at 300 μm. The red circles (lines) and blue circles (lines) represent the estimated $\rho_{2\to3}$ and $\rho_{3\to2}$ from the experiment (simulation), respectively.

As g_{41} grows, C_{41} undergoes a gradual reduction, and the associated localization of TESs is weakened. Both $\rho_{2\to3}$ and $\rho_{3\to2}$ show a slight reduction tendency than those with $\Delta g_{41} = 0$ (see more details on Fig. 4 in the main text), but are kept at a relatively high level (Fig. S7a). As g_{41} reduces, $\rho_{2\to3}$ and $\rho_{3\to2}$ show a reverse tendency (Fig. S7b), and are higher than those with $\Delta g_{41} = 0$ (see more details on Fig. 4 in the main text). The edge-to-edge channel conversion effect of the TESs can tolerate the perturbation up to $|\Delta g_{41}/g_{41}| = 42\%$.

9. The topological phase transition point in *N*-level Harper model

The Harper model can be extended to N-level condition. The Bloch Hamiltonian can be written as

$$H_n(\beta_x,\beta_y)=\begin{bmatrix} k_1(\beta_x) & c & & & & & C_{N1}e^{-i\beta_y} \\ c & k_2(\beta_x) & c & & & & \\ & c & . & . & & & \\ & & . & k_n(\beta_x) & c & & \\ & & & c & . & . & \\ & & & & . & . & c \\ C_{N1}e^{i\beta_y} & & & & & c & k_N(\beta_x) \end{bmatrix}_{N\times N}$$

(S20)

where $k_n(\beta_x)=k_b+\Delta k\cos(\beta_x+2\pi n/N)$ is the onsite energy. The modulation benchmark k_b and modulation amplitude Δk have been mentioned in the main text. $c=0.1k_0$ and C_{N1} are the inter-unit and cross-unit hopping strengths, respectively. C_{N1} is taken as the independent variable to analyze the topological phase transition point from the non-trivial phase to the trivial phase.

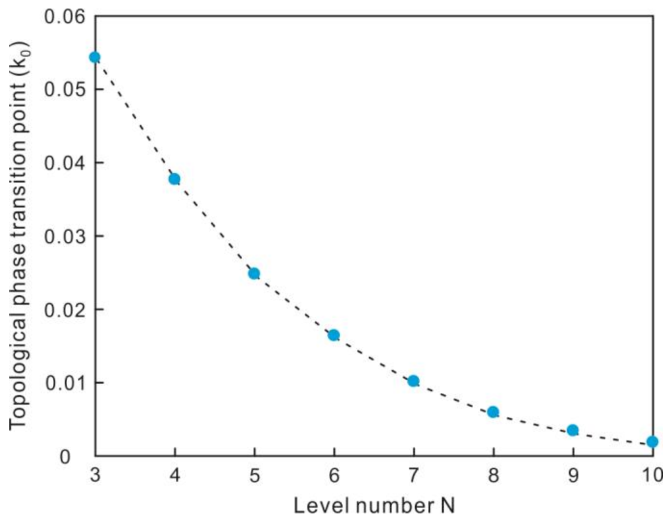

Fig. S8 The topological phase transition points in *N*-level Harper model as C_{N1} is varied. The x axis labels the level number of Harper model. The y axis is the topological phase transition point normalized to k_0, the propagation constant of light in void m mentioned in main text.

We have calculated the topological phase transition points with different level number N. Figure S8 shows that the topological phase transition point is closer to the parameter origin as N is enhanced which indicate a wider range of g_{N1}, the gap distance crossing unit-cell, is allowed for topological protection. The result demonstrates the higher-level Harper model can support TESs in a wider range of cross-unit coupling coefficient C_{N1} compared to that in three or four level Harper model. In other word, higher-level Harper model promises even stronger robustness.